Discontinuous Galerkin methods for solving Boussinesq–Green–Naghdi equations in resolving non-linear and dispersive surface water waves

Nishant Panda [a],*, Clint Dawson [a], Yao Zhang [b], Andrew B. Kennedy [b], Joannes J. Westerink [b], Aaron S. Donahue [b]

[a] *Institute for Computational Engineering and Sciences, University of Texas at Austin, Austin, TX 78712-1229, USA*
[b] *Department of Civil and Environmental Engineering and Earth Sciences, University of Notre Dame, Notre Dame, IN 46556, USA*

A B S T R A C T

A local discontinuous Galerkin method for Boussinesq–Green–Naghdi equations is presented and validated against experimental results for wave transformation over a submerged shoal. Currently Green–Naghdi equations have many variants. In this paper a numerical method in one dimension is presented for the Green–Naghdi equations based on rotational characteristics in the velocity field. Stability criterion is also established for the linearized Green–Naghdi equations for both the analytical problem and the numerical method. Verification is done against a linearized standing wave problem in flat bathymetry and h, p (denoted by K in this paper) error rates are plotted. Validation plots show good agreement of the numerical results with the experimental ones.

© 2014 Elsevier Inc. All rights reserved.

1. Introduction

Surface water wave theory has been an evolving research topic where asymptotic models have been used to resolve wave characteristics. While the shallow water assumption is valid in regions where the characteristic wavelength exceeds a typical depth by orders of magnitude, Boussinesq-type equations have been used to model near-shore wave motion. The basic idea behind all the Boussinesq theories is the introduction of a polynomial representation of the velocity field in the vertical co-ordinate which reduces a $3D$ flow model to a $2D$ flow model. Most of these theories are based on an asymptotic extension of the additional shallow water physics into deeper water to arrive at inviscid, non-linear wave evolution equations. While many models [28,31,32], even though exhibiting good non-linear properties, have limited radius of convergence [24] and are restricted to a finite value of kh_b (k represents a typical wave-number; h_b represents a typical depth), recently some Boussinesq theories [27] have exhibited very high radius of convergence. However, since almost all Boussinesq based models assume an irrotational flow field they are valid up to the breaking point. Since vortices are generated from wave breaking, any model based on irrotational flow will induce large errors in the velocity field.

An alternate approach to the computation of shallow water nonlinear dispersive waves lies in the Green–Naghdi [19,34,36] formulation, where a polynomial structure for the velocity field is retained without any irrotational assumptions. Almost all Green–Naghdi based formulations have been developed in the shallow water limit, although researchers
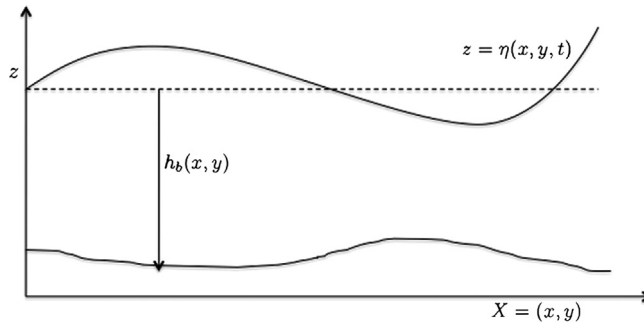

Fig. 1. Domain showing bathymetry and surface elevation.

[38] have successfully extended the formulation to deeper waters. Recently, in [40], the authors developed the Green–Naghdi formulation to arbitrary levels of approximation but also retained the Boussinesq scaling. Such a formulation can be naturally extended to model the surf-zone which is a highly energetic part of the near shore ocean where waves shoal, break and transmit energy to the shore [35,29,23]. Henceforth, in this paper, we refer to these equations as the **R-GN** equations. There are also water wave theories based on the Green–Naghdi approach that employ irrotational characteristics into the velocity formulation. Such systems have been known to provide accurate linear and non-linear dispersion [26,6], and their irrotational assumption brings it more in line with standard Boussinesq systems. We'll refer to these equations as the **I-GN** equations. Since our ultimate goal is to use Green–Naghdi equations to model surf-zone dynamics where we'll need rotational features in the velocity fields to include turbulent/viscous stresses; we'll mainly focus on the R-GN model. The numerical techniques developed for the **R-GN** equations will also apply to the **I-GN** equations.

While Green–Naghdi theory has been identified as a fairly accurate theory that captures non-linear dispersion, there aren't many numerical methods that can be used to solve such equations in an arbitrary grid. Part of this is due to the nature of the Green–Naghdi equations which contain non-linear products of higher-order spatial derivatives and mixed spatio-temporal derivatives. In this paper, we investigate a discontinuous Galerkin method [9] to solve both the R-GN and I-GN equations described above. Even though the R-GN equations are in non-conservative form and contain higher order derivatives, by the use of the local discontinuous Galerkin approximation we can easily handle non-linear products of the derivatives. Moreover, discontinuous Galerkin methods are known to handle complex geometry and extend easily to higher dimensions. Although recently a discontinuous Galerkin (DG) based method has been developed for high order Boussinesq equations [17], at present there are no DG or finite element methods for Green–Naghdi based equations.

In Section 2, we present the physical model, i.e. the R-GN equations due to [40]. Section 3 is devoted to the numerical discretization of these equations using the discontinuous Galerkin method for the spatial approximation. We outline the DG method and comment on the linear and non-linear stability of such an approximation. Finally, we carry out the verification and validation test of our numerical method and conclude with a summary and future work.

2. Governing equations: R-GN equations

Usually, in water wave theory one works with the *non-dimensional* Euler equations for an incompressible fluid. A typical domain is show in Fig. 1. The continuity equation reduces to the *free surface* equation given by,

$$\frac{\partial \eta}{\partial t} + \nabla \cdot \int_{-h_b}^{\eta} \mathbf{u} \, dz = 0, \tag{2.1}$$

where $\eta = \eta(x, y, t)$ is the free surface. The non-dimensional momentum equations, in *Cartesian co-ordinates*, are given by

$$\frac{\partial \mathbf{u}}{\partial t} + \mathbf{u} \cdot \nabla \mathbf{u} + w \frac{\partial \mathbf{u}}{\partial z} + \nabla P = 0. \tag{2.2}$$

$$\mu^2 \frac{\partial w}{\partial t} + \mu^2 \mathbf{u} \cdot \nabla w + \mu^2 w \frac{\partial w}{\partial z} + \frac{\partial P}{\partial z} + g = 0, \tag{2.3}$$

where $\nabla = [\partial/\partial x, \partial/\partial y]^T$, $\mathbf{u} = [u, v]^T$ and μ represents a dimensionless wave number. Integrating (2.3) from z to η, and assuming a zero gauge pressure at the free surface, we find

$$P(z) = \mu^2 \int_z^{\eta} \frac{\partial w}{\partial t} dz + \mu^2 \int_z^{\eta} \mathbf{u} \cdot \nabla w \, dz + \mu^2 \int_z^{\eta} w \frac{\partial w}{\partial z} dz + g(\eta - z). \tag{2.4}$$

In accordance with the classical Boussinesq and Green–Naghdi theory, we follow the recipe outlined in [40] where an approximated velocity field given by

$$\mathbf{u} \approx \bar{\mathbf{u}} = \sum_{n=0}^{N} \mu^{\beta_n} \mathbf{u}_n(x, y, t) f_n(z)$$

is inserted into the equations above to get arbitrary levels of approximation. For the sake of completeness we outline the steps in constructing a Rotational Boussinesq–Green–Naghdi approximation of the Euler equations.

1. Define a level of wave approximation, $O(\mu^N)$.
2. Insert the approximate velocity field into the free surface equation (2.1), retaining all the terms up to the desired level of approximation.
3. Insert the approximate velocity field into the pressure equation (2.4) to get $\bar{P}$.
4. Insert the approximate velocity field into the horizontal momentum equation (2.2). Integrate in weighted residual sense, using the $N + 1$ basis functions used in the approximated velocity field, i.e.

$$\int_{-h_b}^{\eta} f_m \left(\frac{\partial \bar{\mathbf{u}}}{\partial t} + \bar{\mathbf{u}} \cdot \nabla \bar{\mathbf{u}} + \bar{w} \frac{\partial \bar{\mathbf{u}}}{\partial z} + \nabla \bar{P} \right) dz = 0, \quad m = 0 \ldots N \tag{2.5}$$

where $\bar{w}$ represents the approximate vertical velocity field which can be determined from the approximate horizontal velocity field [40].

In this paper we focus mainly on the $O(\mu^2)$ equations. As derived in [40], the approximate velocity field is given by

$$\bar{\mathbf{u}} = \mathbf{u}_0 + \mu^2 \mathbf{u}_1 f_1(q) + \mu^2 \mathbf{u}_2 f_2(q),$$
$$\bar{w} = -\nabla \cdot \mathbf{u}_0 H q - \mathbf{u}_0 \cdot \nabla h_b, \tag{2.6}$$

where q is a sigma-type co-ordinate given by $q = \frac{z + h_b}{h_b + \eta}$ and $H = \eta + h_b(x, y)$ is the *total* water depth. The convergence properties of such an expansion are discussed in [40]. Following the steps above, we end up with the free-surface evolution equation and the momentum equations to solve for η, $\mathbf{u}_0$, $\mathbf{u}_1$ and $\mathbf{u}_2$. $\mathbf{u}_1$, $\mathbf{u}_2$ terms can be thought of as an additional representation of the velocity field over the depth. In other words, keeping $\mathbf{u}_0$, $\mathbf{u}_1$ and $\mathbf{u}_2$ terms we are better able to resolve the variation of velocity field over the depth of the ocean. Moreover, by making these terms independent we are not imposing any irrotational assumptions on the velocity field. The surface elevation equation is given by,

$$\eta_{,t} + \nabla \cdot \left(\mathbf{u}_0 H + \mu^2 \sum_{m=1}^{2} \mathbf{u}_m H c_m \right) = 0. \tag{2.7}$$

The momentum equations are given by,

$$\mathbf{u}_{0,t} H c_1^m + \mathbf{u}_0 \cdot \nabla \mathbf{u}_0 H c_2^m + g \nabla \eta H c_3^m + \mu^2 \sum_{n=1}^{2} \left(\mathbf{u}_{n,t} H c_4^m - \mathbf{u}_n \eta_{,t} c_5^m \right)$$

$$- \mu^2 \left[\frac{1}{2} \nabla (\nabla \cdot \mathbf{u}_{0,t}) H^3 c_6^m + \nabla \cdot \mathbf{u}_{0,t} \nabla H H^2 c_7^m + \nabla (\mathbf{u}_{0,t} \cdot \nabla h_b) H^2 c_8^m \right.$$

$$+ \mathbf{u}_{0,t} \cdot \nabla h_b \nabla \eta H c_9^m - (\nabla \cdot \mathbf{u}_{0,t}) H^2 \nabla h_b c_{10}^m \Big]$$

$$+ \mu^2 \sum_{n=1}^{2} \left[(\mathbf{u}_n \cdot \nabla \mathbf{u}_0 + \mathbf{u}_0 \cdot \nabla \mathbf{u}_n) H c_{11}^m - \mathbf{u}_n \nabla \cdot (\mathbf{u}_0 H) c_{12}^m \right]$$

$$+ \mu^2 H^2 \left[(\nabla \cdot \mathbf{u}_0)^2 - \mathbf{u}_0 \cdot \nabla (\nabla \cdot \mathbf{u}_0) \right] \left(\nabla \eta c_{13}^m + \nabla h_b c_{14}^m \right)$$

$$+ \frac{\mu^2}{2} H^3 \nabla \left[(\nabla \cdot \mathbf{u}_0)^2 - \mathbf{u}_0 \cdot \nabla (\nabla \cdot \mathbf{u}_0) \right] c_{15}^m$$

$$- \mu^2 H \nabla \eta \mathbf{u}_0 \cdot \nabla (\mathbf{u}_0 \cdot \nabla h_b) c_{16}^m - \mu^2 H^2 \nabla \left[\mathbf{u}_0 \cdot \nabla (\mathbf{u}_0 \cdot \nabla h_b) \right] c_{17}^m = 0, \quad \forall m \in [0, 2], \tag{2.8}$$

where all the coefficients c_k^m are defined in Appendix A.

3. Numerical methods

We investigate a *local discontinuous Galerkin* (LDG) method [10,11,4] for the spatial discretization of the Green–Naghdi equations given by (2.7)–(2.8) for the R-GN equations. The resulting semi-discrete equations are then integrated in time using an explicit Runge–Kutta method to evolve the equations from suitable initial conditions. The discontinuous Galerkin

Methods (DG) are locally conservative, stable and high-order methods which can easily handle complex geometries. This feature has made the method attractive in applications to water wave theories [1,13,25,39,18,17]. In this paper we'll only focus on the 1D formulation of the R-GN equations. The full 2D equations will be considered in future work.

Let $\Omega = [0, L]$ be the spatial domain. Define a partition

$$0 = x_{1/2} < x_{3/2} < \ldots < x_{J+1/2} = L,$$

and define,

$$E_j = [x_{j-1/2}, x_{j-1/2}],$$
$$\mathcal{E} = \{x_{j+1/2}\},$$
$$h_j = x_{j+1/2} - x_{j-1/2},$$
$$h = \max_j h_j, \tag{3.1}$$

to be the finite element, set of boundary points, element size and the maximum element size respectively. Construct a set of test functions V_h^K on the partition, consisting of piecewise polynomials of degree K:

$$V_h^K = \{v : v|_{E_j} \in \mathbb{P}_K(E_j) \; \forall j = 1, \ldots, J\}. \tag{3.2}$$

Let us denote,

$$v(x_{j+1/2}^+) = \lim_{\epsilon \to 0^+} v(x_{j+1/2} + \epsilon),$$
$$v(x_{j+1/2}^-) = \lim_{\epsilon \to 0^+} v(x_{j+1/2} - \epsilon).$$

Then, we can define the jump and average of v at the endpoints of E_j as:

$$[|v(x_{j+1/2})|] = v(x_{j+1/2}^-) - v(x_{j+1/2}^+),$$
$$\{v(x_{j+1/2})\} = \frac{1}{2}(v(x_{j+1/2}^-) + v(x_{j+1/2}^+)). \tag{3.3}$$

For any $v \in V_h^K$, we can write v as

$$v = \sum_{j=1}^{J} \sum_{i=0}^{K} \tilde{v}_i^j \phi_i(x), \tag{3.4}$$

where $\{\phi_i\}$ is a basis for $\mathbb{P}_K$. In this paper we chose $\phi_i = P_i$, where P_i is the normalized Legendre polynomial [21]. Given $u^h \in V_h^K$, all derivatives of u^h are calculated in an *LDG* sense described below. Define:

$$\lambda^h = u_x^h,$$
$$\mathbb{B}(\lambda^h, w) = \mathbb{L}_{u^h}(w),$$

where $\mathbb{B} : V_h^K \times V_h^K \to \mathbb{R}$ is the *bi-linear* form and $\mathbb{L}_{u^h} : V_h^K \to \mathbb{R}$ is the *linear* form given by

$$\mathbb{B}(\lambda^h, w) = \sum_j (\lambda^h, w)_{E_j},$$
$$\mathbb{L}_{u^h}(w) = -\sum_j (u^h, w_x)_{E_j} + \langle \hat{u}^h, [|w|] \rangle_{\mathcal{E}}, \tag{3.5}$$

where $w \in V_h^K$ and $(\,,\,)$ denotes the standard L_2 inner product. In a similar fashion, we compute u_{xx}^h, u_{xxx}^h and so on. Looking ahead, let us define the following *bi-linear* form:

$$\mathbb{B}_\sigma(u^h, w) = \sum_j (u^h, w)_{E_j} + \sigma \langle [|u^h|], [|w|] \rangle_{\mathcal{E}}, \tag{3.6}$$

where $\sigma \geq 0$. Note, $\hat{u}^h = F(u^{h-}, u^{h+})$ is the single valued *flux* function evaluated at the edges of E_j. Various flux functions can be found in the DG literature. The simplest flux is the average flux given by:

$$F(u_{j+1/2}^-, u_{j-1/2}^+) = \{u(x_{j+1/2})\}. \tag{3.7}$$

To calculate the inner products we define an affine mapping given by [21]:

$$x \in E_j : \quad x(\xi) = x_{j-1/2} + \frac{1+\xi}{2} h_j. \tag{3.8}$$

This maps $x \mapsto [-1, 1]$, where we utilize the Gaussian quadrature formulae so that the integrals are evaluated exactly.

3.1. Discretization of the R-GN equations

The R-GN equations (2.7)–(2.8) can be written as:

$$\varphi = Rhs_\eta, \tag{3.9a}$$

$$\mathcal{L}[s_0] = Rhs_{u_0}, \tag{3.9b}$$

$$s_1 = Rhs_1, \tag{3.9c}$$

$$s_2 = Rhs_2, \tag{3.9d}$$

where $\varphi = \eta_t$, $s_0 = u_{0,t}$, $s_1 = u_{1,t}$, $s_2 = u_{0,t}$; and $\mathcal{L}$ is an elliptic operator given by $A + B\frac{\partial}{\partial x} - C\frac{\partial^2}{\partial x^2}$, where A, B, C are:

$$A = H\tilde{g}_0 - \mu^2 h_x \eta_x H\tilde{g}_0,$$

$$B = -\mu^2 H^2 H_x \tilde{g}_0 - \mu^2 h_{b,x} H^2 (\tilde{g}_0 - \tilde{s}_0) + \mu^2 H^2 h_{b,x} \tilde{s}_0,$$

$$C = \frac{\mu^2}{2} H^3 (\tilde{g}_0 - \tilde{v}_0). \tag{3.10}$$

Rhs_η, Rhs_{u_0}, Rhs_1 and Rhs_2 are given in (A.2), (A.3), (A.6) and include non-linear products of derivatives of u_0, u_1, u_2, s_0 and η. $\tilde{g}_0$, $\tilde{s}_0$, $\tilde{v}_0$, g_1, g_2 are constants that depend on the type of function $f(q)$ used in (2.6) and g is the non-dimensional gravitational constant. See Appendix A for the complete description of these terms. Note that (3.9b) is similar to the dispersive equation in the I-GN equations.

The weak formulation of the R-GN equations (3.9) is then to find:

$$\varphi^h \in V_h^K,$$

$$s_0^h \in V_h^K,$$

$$s_1^h \in V_h^K,$$

$$s_2^h \in V_h^K,$$

$$r^h \in V_h^K,$$

$$p^h \in V_h^K, \tag{3.11}$$

where r^h, p^h approximate $s_{0,x}$ and $s_{0,xx}$ respectively, such that,

$$\mathbb{B}_\sigma(\varphi^h, \chi) = \mathbb{L}_1(\chi), \tag{3.12a}$$

$$\mathbb{B}_s(s_0^h, \psi) + \mathbb{B}_r(r^h, \psi) + \mathbb{B}_p(-p^h, \psi) = \mathbb{L}_2(\psi), \tag{3.12b}$$

$$\mathbb{B}_\sigma(s_1^h, \phi) = \mathbb{L}_3(\phi), \tag{3.12c}$$

$$\mathbb{B}_\sigma(s_2^h, \omega) = \mathbb{L}_4(\omega), \tag{3.12d}$$

where $\mathbb{B}_\sigma$ is defined in (3.6). $\mathbb{B}_s$, $\mathbb{B}_r$ and $\mathbb{B}_p$ are given by:

$$\mathbb{B}_s(s_0^h, w) = \sum_j (As_0^h, w)_{E_j},$$

$$\mathbb{B}_r(r^h, w) = \sum_j (Br^h, w)_{E_j},$$

$$\mathbb{B}_p(p^h, w) = \sum_j (Cp^h, w)_{E_j}, \tag{3.13}$$

where A, B and C are defined in (3.10). To eliminate, r^h and p^h we define the following equations [2]:

$$\sum_j (r^h, w)_{E_j} = \sum_j (-s_0^h, w_x)_{E_j} + \langle \hat{s}_0^h, [|w|] \rangle_{\mathcal{E}},$$

$$\sum_j (p^h, w)_{E_j} = \sum_j (-r^h, w_x)_{E_j} + \langle \hat{r}^h, [|w|] \rangle_{\mathcal{E}} - \sigma_{11} \langle [|s_0^h|], [|w|] \rangle_{\mathcal{E}}. \tag{3.14}$$

Here σ_{11} is a penalty term and w, χ, ψ, ϕ and $\omega \in V_h^K$. The *linear* forms are given by:

$$\mathbb{L}_1(\chi) = \sum_j \left(Rhs_\eta^h, \chi\right)_{E_j},$$

$$\mathbb{L}_2(\psi) = \sum_j \left(Rhs_{u_0}^h, \psi\right)_{E_j},$$

$$\mathbb{L}_3(\phi) = \sum_j \left(Rhs_1^h, \phi\right)_{E_j},$$

$$\mathbb{L}_4(\omega) = \sum_j \left(Rhs_2^h, \omega\right)_{E_j}. \tag{3.15}$$

The constant σ_{11} is chosen as described in Eq. (3.31) to satisfy the linear stability and is discussed in the following sections. The time stepping algorithm then follows:

→ Given η^h, u_0^h, u_1^h and u_2^h at t^n
  ↪ Compute all the spatial derivatives from (3.5).
  ↪ Determine A, B and C from (3.10), and Rhs_η, Rhs_{u_0}, Rhs_1 and Rhs_2.
  ↪ Compute $\varphi^h = \eta_t^h$ from (3.12a).
  ↪ Compute r^h, p^h in terms of s_0^h from (3.14). Then do the elliptic solve for $s_0^h = u_{0,t}^h$ from (3.12b) and update Rhs_1 and Rhs_2. This will involve the solution of a linear equation.
  ↪ Compute $s_1^h = u_{1,t}^h$ and $s_2^h = u_{2,t}^h$ from (3.12c) and (3.12d) respectively.
→ Update η^h, u_0^h, u_1^h and u_2^h from φ^h, s_0^h, s_1^h and s_2^h respectively,

where each update is performed using a fourth order classical Runge–Kutta method. A similar strategy can be followed to solve the dispersive part of I-GN equations [6].

3.2. Boundary conditions

The boundary conditions in DG methods are generally imposed weakly. The most common boundary conditions that occur when we solve Green–Naghdi equations are wall boundary condition, transmissive boundary condition and periodic boundary conditions. Other specialized boundary conditions will be considered in future work where we will extend our model to include the shoreline, wave breaking, absorption etc. to make it into a surf-zone model.

1. Wall: For wall boundary conditions we take $\mathbf{u}^{ext.} = -\mathbf{u}^{int.}$ and $H^{ext.} = H^{int.}$.
2. Transmissive: We take $\mathbf{u}^{ext.} = \mathbf{u}^{int.}$ and $H^{ext.} = H^{int.}$.
3. Periodic: The domain can be thought to be *wrapped around* and the exterior edge at L corresponds to the interior edge at 0 of the domain.

Here *ext.* and *int.* refer to *exterior* and *interior* respectively.

3.3. Linear and non-linear stability

In this section we will perform a stability analysis of the linearized R-GN equations for a flat bathymetry h_b. For the analytic problem we'll carry out the analysis through Fourier expansion as detailed in [17]. The eigenspectra will be shown to be purely imaginary and bounded. We'll also establish the *flux* criteria for the discrete problem by considering the stability of the numerical solution using the discontinuous Galerkin method. The linearized $O(\mu^2)$ R-GN equations can be written as:

$$\sum_{n=0}^{2} A_{mn}(h_b)u_{n,t} + \left[B_{m0}(h_b)u_{0,xt} + C_{m0}(h_b)u_{0,xxt}\right] + g_m\eta_x = 0, \quad \forall m = 0\ldots 2.$$

$$\eta_t + \sum_{n=0}^{2} \left(D_n(h_b)u_n\right)_{,x} = 0.$$

To keep our analysis simple we choose the shifted Legendre polynomials [40] in (2.6) which decouples u_1 and u_2 above and hence it is sufficient only to look at the following equation:

$$u_{0,t} - c_0 h_b^2 u_{0,xxt} + g\eta_x = 0,$$

$$\eta_t + h_b u_{0,x} = 0. \tag{3.16}$$

Note that by choosing the shifted Legendre polynomials in (2.6) the coefficient of $u_{0,xt}$ becomes 0.

3.3.1. Linear stability of the analytic problem through Fourier analysis

We perform a Fourier stability analysis [17] assuming a harmonic variation in space, $\eta(x,t) = \hat{\eta}(t)e^{ikx}$, $u_0(x,t) = \hat{u}_0(t)e^{ikx}$. Inserting this into (3.16), we get:

$$\mathbf{U}_t = Q\,\mathbf{U},$$

where $\mathbf{U} = [\hat{u}_0, \hat{\eta}]^T$ and $Q = A^{-1}B$ where, A and B are given by:

$$A = \begin{bmatrix} 1 + c_0 h_b^2 k^2 & 0 \\ 0 & 1 \end{bmatrix}$$

$$B = \begin{bmatrix} 0 & -igk \\ ikh_b & 0 \end{bmatrix}$$

The eigenvalues of Q can be found to be

$$\lambda(Q) = \pm i \sqrt{\dfrac{g/h_b}{c_0 + \dfrac{1}{(kh_b)^2}}}$$

To obtain a bound of the magnitude we look at $\lim_{kh_b \to \infty} |\lambda(Q)|$. This gives us $|\lambda_{\max}| = \sqrt{1/c_0}\sqrt{g/h_b}$, where $c_0 = 1/6$.

3.3.2. Linear stability of the numerical method

Let us rewrite (3.16) as a system of first order (in space) equations:

$$r - u_{0,xt} = 0, \tag{3.17a}$$

$$u_{0,t} - c_0 h_b^2 r_{,x} + g\eta_{,x} = 0, \tag{3.17b}$$

$$\eta_{,t} + h_b u_{0,x} = 0. \tag{3.17c}$$

For simplicity let us assume $u(0) = u(L) = 0$. Adding (3.17c) and (3.17b) and subtracting (3.17a) after multiplication by $g\eta$, $h_b u_0$ and $c_0 h_b^3 u_{0,x}$ respectively and integrating from 0 to L we get:

$$g(\eta_{,t}, \eta) + h_b(u_{0,t}, u_0) + c_0 h_b^3 (u_{0,xt}, u_{0,x}) = 0.$$

Hence, to show stability of the numerical method it is sufficient to show [12]

$$g(\eta_{,t}^h, \eta^h) + h_b(u_{0,t}^h, u_0^h) + c_0 h_b^3 (u_{0,xt}^h, u_{0,x}^h) + \Theta = 0,$$

where Θ is such that integrating in time we achieve the desired stability. In the following paragraphs we will show the *discrete* time stability of the linearized equations.

For simplicity let us drop all the coefficients and let $u_0 = u$. Then, working with the discrete versions of (3.17a), (3.17b) and (3.17c) our numerical method is given by

$$\left(r^h, v\right)_\Omega = \left(u_{xt}^h, v\right)_\Omega \tag{3.18}$$

$$\left(u_t^h, w\right)_\Omega = -\left(r^h, w_x\right)_\Omega + \langle \hat{r}^h, [\![w]\!]\rangle_\mathcal{E} - \sigma_{11}\langle [\![u_t^h]\!], [\![w]\!]\rangle_\mathcal{E} + \left(\eta^h, w_x\right)_\Omega - \langle \hat{\eta}^h, [\![w]\!]\rangle_\mathcal{E} \tag{3.19}$$

$$\left(\eta_t^h, p\right)_\Omega = \left(u^h, p_x\right)_\Omega - \langle \hat{u}^h, [\![p]\!]\rangle_\mathcal{E} \tag{3.20}$$

where $v, w, p \in V_h^K$. Let

$$v = u_x^h,$$

$$w = u^h,$$

$$p = \eta^h.$$

Thus, for an element E_j, we get,

$$\left(r^h, u_x^h\right)_{E_j} = \left(u_{xt}^h, u_x^h\right)_{E_j} \tag{3.21}$$

$$\left(u_t^h, u^h\right)_{E_j} = -\left(r^h, u_x^h\right)_{E_j} + \hat{r}^h u^h \big|_{x_{j-1/2}}^{x_{j+1/2}} - \sigma_{11}[\![u_t^h]\!]u^h \big|_{x_{j-1/2}}^{x_{j+1/2}} + \left(\eta^h, u_x^h\right)_{E_j} - \hat{\eta}^h u^h \big|_{x_{j-1/2}}^{x_{j+1/2}} \tag{3.22}$$

$$\left(\eta_t^h, \eta^h\right)_{E_j} = \left(u^h, \eta_x^h\right)_{E_j} - \hat{u}^h \eta^h \big|_{x_{j-1/2}}^{x_{j+1/2}} \tag{3.23}$$

Hence, we get the following:

$$\left(\eta_t^h, \eta^h\right)_{E_j} + \left(u_t^h, u^h\right)_{E_j} + \left(u_{xt}^h, u_x^h\right)_{E_j} + \Theta_{E_j} = \hat{r}^h u^h \big|_{x_{j-1/2}}^{x_{j+1/2}} \tag{3.24}$$

where Θ_{E_j} is given by:

$$-\int_{E_j} d(\eta^h u^h) + \hat{\eta}^h u^h|_{x_{j-1/2}}^{x_{j+1/2}} + \hat{u}^h \eta^h|_{x_{j-1/2}}^{x_{j+1/2}} + \sigma_{11}[|u_t^h|]u^h|_{x_{j-1/2}}^{x_{j+1/2}} \tag{3.25}$$

Adding over the elements we get:

$$(\eta_t^h, \eta^h) + (u_t^h, u^h) + (u_{xt}^h, u_x^h) + \Theta = \langle \hat{r}^h, [|u^h|]\rangle_{\mathcal{E}}, \tag{3.26}$$

where $\Theta = \mathcal{I} + \mathcal{II} + \mathcal{B}.\mathcal{T}$. We see that $\mathcal{I}, \mathcal{II}$ are given by:

$$\mathcal{I} = \sum_{\mathcal{E}_i}([|u_0^h|](\hat{\eta}^h - \{\eta^h\}) + [|\eta^h|](\hat{u}_0^h - \{u_0^h\})),$$

$$\mathcal{II} = \sigma_{11}\langle[|u_t^h|], [|u^h|]\rangle_{\mathcal{E}}.$$

The boundary terms $\mathcal{B}.\mathcal{T}$ are given by,

$$-(\eta^h u_0^h)^-|_L + (\eta^h u_0^h)^+|_0$$
$$+\hat{\eta}^h(u_0^h)^-|_L - \hat{\eta}^h(u_0^h)^+|_0$$
$$+\hat{u}_0^h(\eta^h)^-|_L - \hat{u}_0^h(\eta^h)^+|_0$$

Here, $\mathcal{E}_i$ represents the set of interior edges. From the above expressions it is easy to see that if we choose $\hat{u}_0^h = \{u_0^h\}$, $\hat{\eta}^h = \{\eta^h\}$ and $\hat{u}_0^h = 0$, $\hat{\eta}^h = \eta^{h\pm}$ at the boundaries $\mathcal{I}$ and $\mathcal{B}.\mathcal{T}$ become zero. Thus to get the desired stability we have to bound $\langle \hat{r}^h, [|u^h|]\rangle_{\mathcal{E}}$. Note that if u^h were continuous in the domain then this term would be zero.

In the following paragraphs we will carry out the discrete time stability. Let us introduce some notation,

$$u_{xt}^h[n] = \frac{u_x^h[n] - u_x^h[n-1]}{\delta t} \qquad u_t^h[n] = \frac{u^h[n] - u^h[n-1]}{\delta t} \tag{3.27}$$

where n is the current *time* level.

We can then find a lower bound for the *LHS* of Eq. (3.26) given by the following:

$$(u_{xt}^h[n], u_x^h[n])_\Omega = \frac{1}{2\delta t}\left[\|u_x^h[n]\|_{L^2(\Omega)}^2 - \|u_x^h[n-1]\|_{L^2(\Omega)}^2 + \|u_x^h[n] - u_x^h[n-1]\|_{L^2(\Omega)}^2\right]$$

$$(u_t^h[n], u^h[n])_\Omega \geq \frac{1}{2\delta t}\left[\|u^h[n]\|_{L^2(\Omega)}^2 - \|u^h[n-1]\|_{L^2(\Omega)}^2\right]$$

$$\frac{\sigma_{11}}{\delta t}\langle[|u^h[n] - u^h[n-1]|], [|u^h[n]|]\rangle_{\mathcal{E}} \geq \frac{\sigma_{11}}{2\delta t}\left[\|[|u^h[n]|]\|_{L^2(\mathcal{E})}^2 - \|[|u^h[n-1]|]\|_{L^2(\mathcal{E})}^2\right]$$

For the *RHS* of Eq. (3.26) after dropping the index n, we can find an upper bound given by:

$$\langle \hat{r}^h, [|u^h|]\rangle_{\mathcal{E}} \leq \|\hat{r}^h\|_{L^2(\mathcal{E})}\|[|u^h|]\|_{L^2(\mathcal{E})} \quad \text{from Cauchy–Schwarz inequality}$$

$$= \sigma_{11}^{-1/2}\|\hat{r}^h\|_{L^2(\mathcal{E})}\sigma_{11}^{1/2}\|[|u^h|]\|_{L^2(\mathcal{E})} \quad \text{multiplying and dividing by } \sigma_{11}^{1/2}$$

$$\leq \frac{1}{2}\left(\frac{\sigma_{11}^{-1}}{\epsilon_1}\|\hat{r}^h\|_{L^2(\mathcal{E})}^2 + \epsilon_1\sigma_{11}^1\|[|u^h|]\|_{L^2(\mathcal{E})}^2\right)$$

$$\leq \epsilon\sigma_{11}^{-1}\|r^h\|_{L^2(\Omega)}\|r^h\|_{H^1(\Omega)} + \frac{1}{2}\epsilon_1\sigma_{11}\|[|u^h|]\|_{L^2(\mathcal{E})}^2 \quad \text{trace inequality of the first term}$$

$$\leq C_1\sigma_{11}^{-1}h_{\min}^{-1}\|r^h\|_{L^2(\Omega)}^2 + \frac{1}{2}\epsilon_1\sigma_{11}\|[|u^h|]\|_{L^2(\mathcal{E})}^2 \quad \text{inverse inequality of the first term}$$

$$\leq C_1\sigma_{11}^{-1}h_{\min}^{-1}\|u_{xt}^h\|_{L^2(\Omega)}^2 + \frac{1}{2}\epsilon_1\sigma_{11}\|[|u^h|]\|_{L^2(\mathcal{E})}^2$$

$$= C_1\sigma_{11}^{-1}h_{\min}^{-1}\left\|\frac{u_x^h[n] - u_x^h[n-1]}{\delta t}\right\|_{L^2(\Omega)}^2 + \frac{1}{2}\epsilon_1\sigma_{11}\|[|u^h|]\|_{L^2(\mathcal{E})}^2$$

Here we used the *trace inequality* [7] given by:

$$\|\hat{r}^h\|_{L^2(\mathcal{E})} \leq C_\Omega^t\|r^h\|_{L^2(\Omega)}^{1/2}\|r^h\|_{H^1(\Omega)}^{1/2} \tag{3.28}$$

and the inverse inequality [7]

$$\left\|r^h\right\|_{H^1(E_j)} \leq h_j^{-1} C_{E_j}^i \left\|r^h\right\|_{L^2(E_j)} \tag{3.29}$$

The trace constant C_Ω^t is known to be finite in regular meshes and the constant from inverse inequality $C_{E_j}^i$ is independent of h_j.

Thus collecting all the terms from above, Eq. (3.26) at time level n becomes:

$$\mathcal{L}_1 \leq \frac{1}{2}\epsilon_1\sigma_{11}\left\|\left[\left|u^h[n]\right|\right]\right\|_{L^2(\mathcal{E})}^2, \tag{3.30}$$

where $\mathcal{L}_1$ is given by

$$\begin{aligned}
\mathcal{L}_1 = {} & \frac{1}{2\delta t}\left[\left\|u^h[n]\right\|_{L^2(\Omega)}^2 - \left\|u^h[n-1]\right\|_{L^2(\Omega)}^2\right] \\
& + \frac{\sigma_{11}}{2\delta t}\left[\left\|\left[\left|u^h[n]\right|\right]\right\|_{L^2(\mathcal{E})}^2 - \left\|\left[\left|u^h[n-1]\right|\right]\right\|_{L^2(\mathcal{E})}^2\right] \\
& + \frac{1}{2\delta t}\left[\left\|u_x^h[n]\right\|_{L^2(\Omega)}^2 - \left\|u_x^h[n-1]\right\|_{L^2(\Omega)}^2 + \left(\frac{1}{2} - \frac{C_1\sigma_{11}^{-1}h_{\min}^{-1}}{\delta t}\right)\left\|u_x^h[n] - u_x^h[n-1]\right\|_{L^2(\Omega)}^2\right]
\end{aligned}$$

The above condition imposes the restrictions on σ_{11} for linear stability, i.e.

$$\sigma_{11} \geq \frac{2C_1}{h_{\min}\delta t}, \tag{3.31}$$

where C_1 contains the constants from inverse inequality and the trace inequality.

Thus summing over *time* from $n = 1$ to $n = N$ and multiplying by δt throughout we get

$$\begin{aligned}
& \left\|u^h[N]\right\|_{L^2(\Omega)}^2 + \left\|u_x^h[N]\right\|_{L^2(\Omega)}^2 + 2\sigma_{11}\left\|\left[\left|u^h[N]\right|\right]\right\|_{L^2(\mathcal{E})}^2 + \Theta_N \\
& \qquad \leq \left\|u^h[0]\right\|_{L^2(\Omega)}^2 + \left\|u_x^h[0]\right\|_{L^2(\Omega)}^2 + 2\sigma_{11}\left\|\left[\left|u^h[0]\right|\right]\right\|_{L^2(\mathcal{E})}^2 + \delta t\left(\epsilon_1\sigma_{11}\sum_{n=1}^N\left\|\left[\left|u^h[n]\right|\right]\right\|_{L^2(\mathcal{E})}^2\right),
\end{aligned}$$

where Θ_N is given by

$$\Theta_N = 2\delta t\left(\frac{1}{2} - \frac{C_1\sigma_{11}^{-1}h_{\min}^{-1}}{\delta t}\right)\sum_{n=1}^N\left[\left\|u_x^h[n] - u_x^h[n-1]\right\|_{L^2(\Omega)}^2\right] \tag{3.32}$$

Thus from *discrete Gronwall's* inequality [3] we get the desired stability.

3.3.3. Comments on non-linear stability

The stability analysis for the complete non-linear equations is quite complicated and will be considered in future work. However, similar flux choices as derived above can be used in the non-linear equations. Hence, we take the *average* fluxes to calculate derivatives in the complete non-linear equations. The rotational velocity field characteristic of the Boussinesq–Green–Naghdi equations gives a coupled system of u_0, u_1, u_2 and η and hence makes it extremely challenging to construct a stable numerical scheme. To add additional stability we add *jumps* in the time derivatives of the solution variables which is reflected in the *bi-linear* forms (3.6). To justify this, consider the equation $s_1 = Rhs_1$ where s_1 is the time derivative of u_1. The Rhs_1 terms contain non-linear products of *higher* order derivatives of u_0. If we use first order polynomials to approximate third order derivatives, Rhs_1 will be ill-resolved which in turn will incur errors in s_1 and will cause instability as we update in time. Thus, instead of solving the weak form of $s_1 = Rhs_1$, we modify it as is given in (3.12) by choosing the bi-linear form described in (3.6). This modified weak form can be thought of as adding penalty to φ, s_1 and s_2 terms which are the time derivatives of η, u_1 and u_2 respectively. Since these variables are unknown at time of update we must solve a linear system for φ, s_1 and s_2 at every time step. Note that as we increase our polynomial order we resolve the right hand terms better but still small errors get amplified when long time integration is performed. The penalty parameter σ is chosen to be a positive number. In order to remove *aliasing* errors that can arise out of insufficient quadrature [22] all our spatial integration involving polynomials are carried out exactly. However, in cases of extreme non-linearity high order polynomial approximation may still become unstable. In those cases additional stability through filtering may be needed. An excellent overview of such filters is given in [17,16].

Note that (2.7) is a first order hyperbolic equation in surface elevation (η). There are many ways to tackle the spatial derivatives in such an equation. However, it was observed that a standard treatment of the derivatives as is done in the discretization of hyperbolic problems proved to be unstable. In other words, since the momentum and surface elevation equations are coupled, all spatial derivatives must be discretized in a *compatible* way. In our case we found that treating the spatial derivatives of surface elevation equation as the product of standard non-conservative terms yielded the necessary stability. The usual flux scheme like the local Lax–Friedrichs etc., which are used to handle fluxes (in conservative forms) in hyperbolic equations, did not provide the necessary stability. We must point out that in the *DG* scheme proposed in this paper, polynomial order $K = 0$, i.e. approximating solutions using piecewise constants also resulted in an unstable solution.
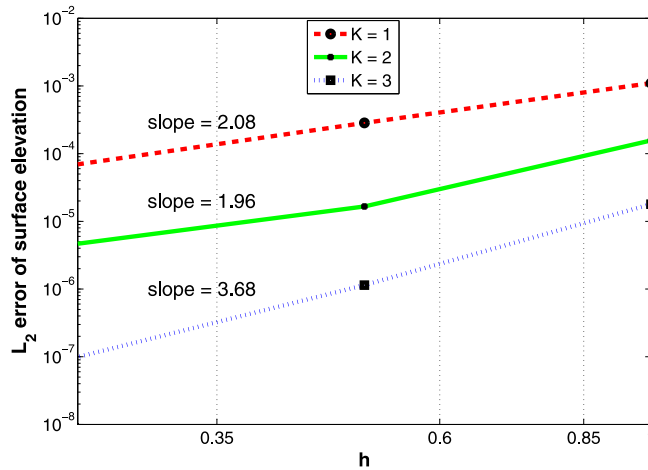
Fig. 2. L_2 error convergence plots for the linearized equations.

4. Verification and validation

To verify our numerical method we consider a linear standing wave problem, where it is known that the mean water level defined by $\frac{1}{L}\int_0^L \eta\,dx = 0$ and an exact solution for flat bathymetry exists based on linear assumption [14]. We present h and K error convergence rates for our verification. To validate our numerical model, we compare the numerical solution of R-GN equations against experimental results obtained for the transformation of a wave train over a trapezoidal shoal. Here, we use the data reported in [5] and [15]. Such a test has been a standard validation scheme for the numerical models based on Boussinesq and Green–Naghdi type wave models as it tests not only linear dispersion and shoaling but also non-linear shoaling and fissioning. We also validate our numerical method against a non-linear solitary wave reflection problem, with experimental results obtained from [33]. We use a polynomial order $K = 1$ in all our simulations.

4.1. Linear standing wave

The R-GN equations as such don't have any known exact analytic solutions. However it is known that for horizontal bottoms [14], a linear standing wave solution exists. We choose a linear standing wave given by $a/h_b = 0.01$, and impose wall boundary conditions and the following initial conditions:

$$\eta(x,0) = a\cos kx,$$
$$u_0(x,0), u_1(x,0), u_2(x,0) = 0, \tag{4.1}$$

where a and k represent the amplitude and wave-number ($2\pi/L$) respectively. The domain $L = 5$ m. The linearized Boussinesq equation for a standing wave admits an exact solution given by

$$\eta = a\cos(kx)\cos(\sigma t).$$

In Fig. 2 we plot the L_2 error of the **linearized** R-GN equations like (3.16) but with monomial shape functions for the velocity expansion. We can immediately see the optimal $K + 1$ convergence for odd polynomial order and suboptimal K convergence for even polynomial order whenever the penalty parameter σ_{11} is chosen to satisfy linear stability.

However, obtaining the convergence rates for the complete non-linear equations is quite cumbersome mainly because there are no known exact solutions for the non-linear R-GN equations and even constructing a manufactured solution is non-trivial. To study the convergence properties of the non-linear equations we use the initial conditions as above but for $K = 1$ we consider the *true* solution to be as given by the simulation run on $K = 1$, $h = 1/8$ and similarly for $K = 2$ we consider the true solution to be as given by $K = 2$, $h = 1/8$. We then get the h convergence plot by running the simulation for $T = 1$ seconds on grids of $h = 1, 1/2, 1/4$. The time step δt is given by $\delta t = \frac{1}{2*K+1} * \frac{h}{C}$ where C is the linear wave speed [14]. Note that getting error convergence plots for $K \geq 3$ is very tedious due to the elliptic solve required in each time step. Moreover, the condition number increases as h is refined and K is increased and hence getting a suitable CFL criteria for time stepping becomes challenging. In Fig. 3 we observe similar convergence rates as for the linear case.

4.2. Transformation of a wave train over a submerged shoal

In this experiment first performed in [5], a wave train propagates towards a submerged trapezoidal shoal. Linear behavior is exhibited before the bar, while non-linear shoaling causes steepening as the waves interact with the slope. Complex multi-frequency waves are generated after the bar as bound harmonics are released in deeper water at the top of the
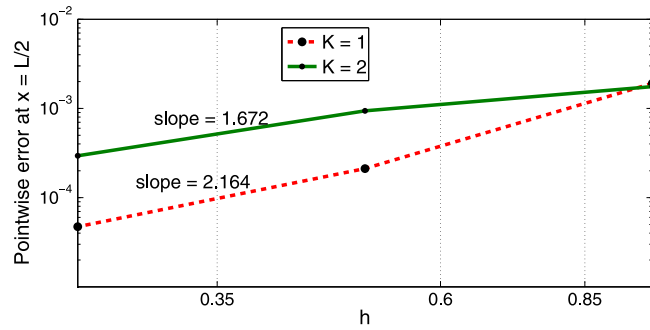
Fig. 3. Pointwise error convergence plots for the non-linearized equations.
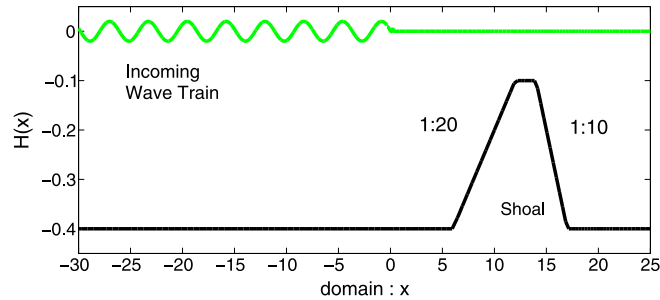

Fig. 4. Initial configuration for validation case.

bar. As the waves propagate onto the front slope of the bar, nonlinear interactions transfer energy from the leading wave component to higher harmonics, causing the wave to become steeper. After the peak of the bar is reached and the bottom slope becomes negative, the nonlinear coupling of the higher harmonics with the fundamental wave becomes progressively weaker, and, from higher to lower harmonics, each of the Fourier components are released as free waves with their own bound higher harmonics. Hence, this experiment tests both the linear dispersion (after the bar) and the non-linear characteristics of the model.

The initial wave train has a period of $T_p = 2.02$ s and wave height $2a = 2$ cm. The mean water depth is $h_b = 0.4$ m. The initial configuration is shown in Fig. 4. A *non-uniform* grid is used where the grid spacing decreases linearly from $h = 0.3$ m at $x = 0$ to $h = 0.1$ m at $x = 12$ and remains 0.1 m till $x = 25$ m. The *CFL* number is taken as $1/(2K + 1)$, where K is the polynomial order, and δt is calculated using the shallow water speed $c = \sqrt{gh_b}$. The numerical results are validated against the experimental test as shown in the plots in Fig. 5. Fig. 6 depicts the linear dispersion where the non-dimensional wave speed is plotted against the non-dimensional frequency [20]. The vertical dotted lines indicate the location of the frequency of the fundamental wave, of which the period is $T_1 = 2.02$ s, and its harmonics with periods $T_2 = T_1/2$, $T_3 = T_1/3$ and so on. As the bound waves are released as free waves, they travel with their own speed which, in the linear limit, are represented by the intersection of the vertical lines T_2, T_3, etc. with the present model's dispersion curve. As inferred from the plot, we don't expect the $O(\mu^2)$ model to give perfect agreement for the higher harmonics after the bar. This is reflected from the surface elevation plot at $x = 19.0$ m in Fig. 5. In Fig. 7 we compare the results from the R-GN model with the results from using a shallow water model at $x = 17.3$ m in the same grid and using the same polynomial order $K = 1$. As we can see we miss the dispersion characteristics when using a shallow water model. Moreover, to account for the sharp change in bathymetry we need to utilize a *slope limiter* [12]. Here we have used the simplest min-mod limiter. Hence, the shallow water results are a little dissipative.

4.3. Wave reflection of solitary wave from a vertical wall

Solitary wave reflection exhibits complex non-linear and dispersive phenomena and has been used as a validation case for numerous numerical models based on Boussinesq–Green–Naghdi equations. Experimental observations in [37,8,30] revealed that solitary waves emerging from a collision, in addition to having experienced changes in their phases, were trailed by a dispersive wave train. Moreover, for large amplitudes, the maximum run-up was observed to be higher than those determined from linear theory.

In this numerical study we follow the numerical setup of [33]. The initial conditions are [6]:

$$\eta(x, 0) = a \operatorname{sech}^2 \big(\kappa (x - x_0 - ct) \big),$$
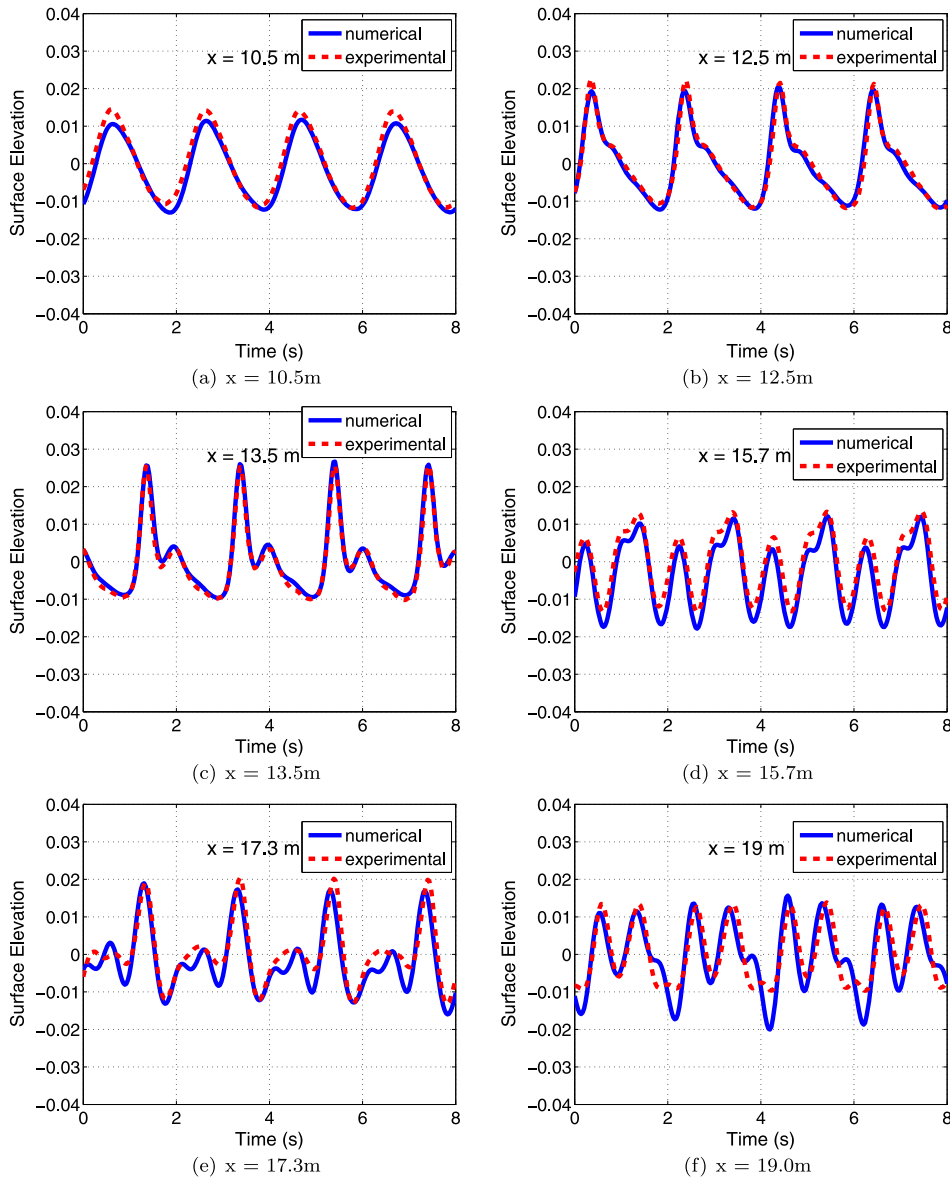$$u_0(x, 0) = c \left(1 - \frac{h_b}{\eta + h_b} \right),$$

Fig. 5. Comparison of experimental and numerical surface elevation variation at different locations around the shoal.

$$u_1(x, 0) = u_2(x, 0) = 0,$$
$$\kappa = \frac{\sqrt{3a}}{2h_b\sqrt{h_b + a}},$$
$$c = \sqrt{g(h_b + a)}.$$

The initial velocity is such that continuity is satisfied at $t = 0$ and the initial configuration is shown in Fig. 8. As the solitary wave moves closer to the wall where the reflection takes place, its amplitude as well as its phase velocity increases quite rapidly. When the wave crest reaches the wall, it doesn't immediately reflect back. There is phase lag during which the amplitude increases to more than double the initial amplitude. This maximum run-up against a vertical wall is compared against experimental results of [30,8] reported in [33] in Fig. 9. A uniform grid of $h = 0.5$ is used and a polynomial order of $K = 1$ is taken. The numerical results agree well with the experimental data.

5. Conclusion

In this work we developed a new local discontinuous Galerkin finite element method to solve Green–Naghdi equations in modeling non-linear and dispersive water waves. We considered the numerical discretization scheme for the Green–Naghdi
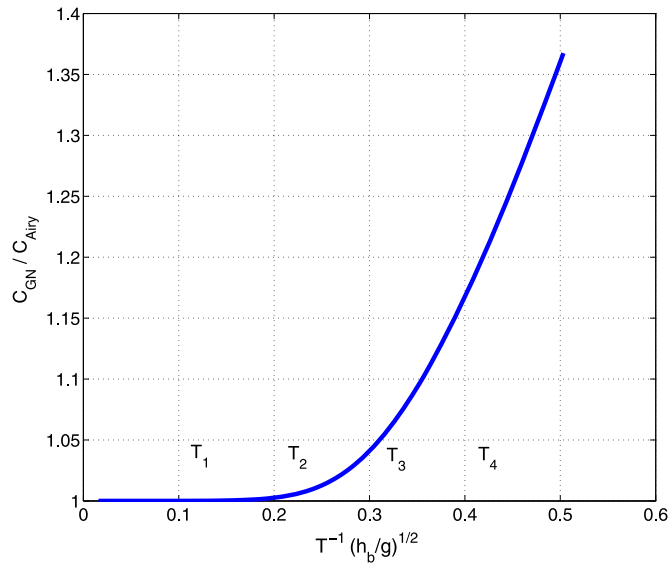
Fig. 6. Linear dispersion relationship as nondimensional wave speed vs. wave frequency. Vertical lines are waves with periods $T_n = 2.02/n$ s.
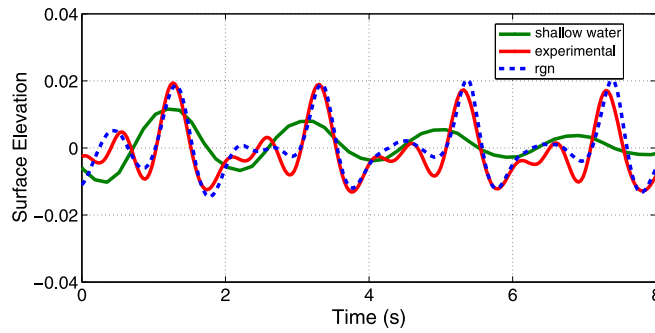

Fig. 7. Comparison of R-GN model, shallow water model and experimental result at $x = 17.3$ m.
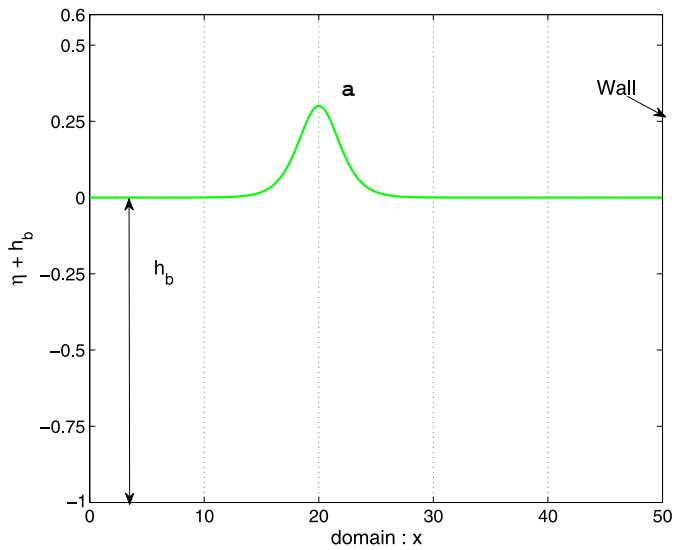

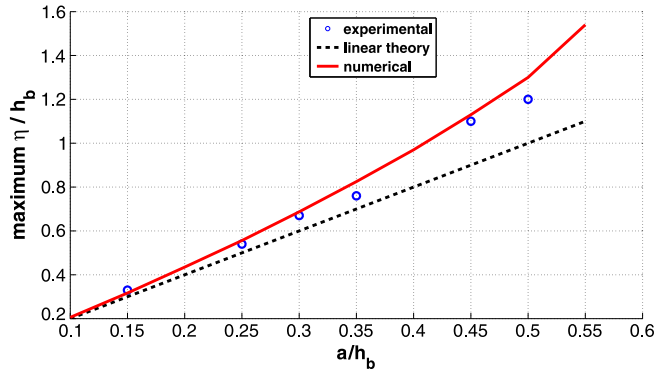
Fig. 8. Initial configuration for the validation case.

Fig. 9. Maximum surface elevation vs. the initial amplitude.

Table A.1
Integrals based on the shape function.

$g_n = \int f_n dq$	$r_n = \int f_n' q dq$	$G_n = \int g_n dq$
$R_n = \int r_n dq$	$\phi_{mn} = \int f_m f_n dq$	$\gamma_{mn} = \int f_m g_n dq$
$\rho_{mn} = \int f_m r_n dq$	$\Gamma_{mn} = \int f_m G_n dq$	$\Theta_{mn} = \int f_m R_n dq$
$\theta_{mn} = \int f_m g_n q dq$	$v_m = \int q^2 f_m dq$	$S_m = \int q f_m dq$
$\epsilon_{mn} = \int f_m f_n' q dq$	$\Psi_{mn} = \int f_m f_n q dq$	$F_{mn} = \int f_m r_n q dq$

equations, namely the **R-GN** and remarked on developing a similar scheme based on the local discontinuous Galerkin method for the **I-GN** model.

A careful stability analysis based on the Fourier transformation was then carried out for the linearized R-GN equations. The eigenspectra was found to be complex and the magnitude was bounded. *Flux criterion* for the numerical method was then established from the stability analysis of the numerical method based on the discontinuous Galerkin framework and important bound on the penalty parameter was established to maintain linear stability. A general non-linear stability analysis has been left for future work, however, a few comments on achieving long time stability were also presented. In general, high order approximation for extremely non-linear cases need additional stability which may render the scheme *inconsistent*. However lower order approximations have been observed to be stable provided the correct bi-linear forms are used as defined in (3.6).

The final part consisted of verification and validation of the R-GN model. A linear standing wave in a flat bathymetry with known exact solution was used for the verification of the linearized equations. Pointwise error at $x = L/2$ was used to compare solutions with different mesh refinement and polynomial order for the complete non-linear R-GN equations. Error plots were shown to give optimal/sub-optimal h, K convergence rates. For validation, wave transformation over a submerged shoal and solitary wave reflection from a vertical wall were chosen and the numerical results show good agreement with the experimental values. Such validation schemes have been standard benchmarks to test not only linear dispersion properties but also complex non-linear transformations.

Although Green–Naghdi equations have been used to model complex non-linear and dispersive water wave characteristics, the inclusion of non-linear products of higher order derivatives in *non-conservative* form has made it cumbersome for the development of numerical schemes in non-uniform grids. The present numerical method hopes to remove this difficulty in using Green–Naghdi based models for modeling near-shore phenomenon. Future work will include the complete 2D equations, wave breaking, generation and absorption boundaries, shoreline theories and sediment transport to construct a true surf-zone model.

Acknowledgements

Appendix A. R-GN equations in 1 and 2 dimensions

In this section, we'll complete the description of the R-GN equations. As described in (2.6), the approximated velocity field is expanded in the *shape functions* $f_n(q)$, where q is a non-dimensional parameter that varies from 0 at the bottom to 1 at the surface elevation. Based on a given shape function $f_n(q)$, Table A.1 gives some useful integral definitions [40].

Using these, we can define the constants introduced in (2.7) and (2.8).

$$c_1 = g_1$$
$$c_2 = g_2$$
$$c_1^m = c_2^m = c_3^m = g_m$$
$$c_4^m = \phi_{mn}; \qquad c_5^m = \epsilon_{mn}; \qquad c_6^m = g_m - \nu_m$$
$$c_7^m = g_m; \qquad c_8^m = g_m - S_m; \qquad c_9^m = g_m; \qquad c_{10}^m = S_m$$
$$c_{11}^m = \phi_{mn}; \qquad c_{12}^m = \epsilon_{mn}; \qquad c_{13} = g_m$$
$$c_{14}^m = g_m - S_m; \qquad c_{15}^m = g_m - \nu_m; \qquad c_{16}^m = g_m; \qquad c_{17}^m = g_m - S_m \qquad\qquad\text{(A.1)}$$

where all the integrals defined in the table are evaluated at $q = 1$. For the 1D R-GN equations introduced in (3.9), we get the following terms:

Rhs_η is given by:

$$-\left(u_0 H_{,x} + u_{0,x} H + \mu^2 g_1 u_1 H_{,x} + \mu^2 g_1 u_{1,x} H + \mu^2 g_2 u_2 H_{,x} + \mu^2 g_2 u_{2,x} H\right) \qquad\qquad\text{(A.2)}$$

Rhs_{u_0} is given by:

$$-\big(d_0 u_0 u_{0,x} + e_0 u_{0,x}^2 + f_0 u_0 u_{0,xx} + h_0 u_{0,x} u_{0,xx} + i_0 u_0 u_{0,xxx}$$
$$+ j_0 u_0^2 + k_0 u_1 u_{0,x} + l_0 u_0 u_{1,x} + n_0 u_2 u_{0,x} + o_0 u_0 u_{2,x}$$
$$+ p_0 u_1 u_0 + q_0 u_2 u_0 + r_0 u_1 + t_0 u_2 + v_0 g \eta_{,x}\big) \qquad\qquad\text{(A.3)}$$

Rhs_{u_1} is given by:

$$-\big(a_1 s_0 + b_1 s_{0,x} + c_1 s_{0,xx} + d_1 u_0 u_{0,x} + e_1 u_{0,x}^2 + f_1 u_0 u_{0,xx}$$
$$+ h_1 u_{0,x} u_{0,xx} + i_1 u_0 u_{0,xxx} + j_1 u_0^2 + k_1 u_1 u_{0,x} + l_1 u_0 u_{1,x}$$
$$+ n_1 u_2 u_{0,x} + o_1 u_0 u_{2,x} + p_1 u_1 u_0 + q_1 u_2 u_0 + r_1 u_1 + t_1 u_2 + v_1 g \eta_{,x}\big) \qquad\qquad\text{(A.4)}$$

Rhs_{u_2} is given by:

$$-\big(a_2 s_0 + b_2 s_{0,x} + c_2 s_{0,xx} + d_2 u_0 u_{0,x} + e_2 u_{0,x}^2 + f_2 u_0 u_{0,xx}$$
$$+ h_2 u_{0,x} u_{0,xx} + i_2 u_0 u_{0,xxx} + j_2 u_0^2 + k_2 u_1 u_{0,x} + l_2 u_0 u_{1,x}$$
$$+ n_2 u_2 u_{0,x} + o_2 u_0 u_{2,x} + p_2 u_1 u_0 + q_2 u_2 u_0 + r_2 u_1 + t_2 u_2 + v_2 g \eta_{,x}\big) \qquad\qquad\text{(A.5)}$$

Rhs_1 and Rhs_2 are given by:

$$Rhs_1 = \frac{\phi_{12} Rhs_{u_2} - \phi_{22} Rhs_{u_1}}{\phi_{12}\phi_{21} - \phi_{22}\phi_{11}}$$
$$Rhs_2 = \frac{\phi_{21} Rhs_{u_1} - \phi_{11} Rhs_{u_2}}{\phi_{12}\phi_{21} - \phi_{22}\phi_{11}} \qquad\qquad\text{(A.6)}$$

For $m = 0$, the coefficients are given as:

$$d_m = H g_m - \mu^2 H \eta_{,x} h_{b,x} \tilde{g}_m + (3 h_{b,xx})\left(-\mu^2 H^2 (\tilde{g}_m - \tilde{S}_m)\right)$$
$$e_m = \mu^2 H^2 \eta_{,x} \tilde{g}_m$$
$$f_m = -\mu^2 H^2 \left(\eta_{,x} \tilde{g}_m + 2(\tilde{g}_m - \tilde{s}_m) h_{b,x}\right)$$
$$h_m = +\frac{\mu^2}{2} H^3 (\tilde{g}_m - \tilde{\nu}_m)$$
$$i_m = \frac{-\mu^2}{2} H^3 (\tilde{g}_m - \tilde{\nu}_m)$$
$$j_m = -\mu^2 H \eta_{,x} h_{b,xx} \tilde{g}_m - h_{b,xxx} \mu^2 H^2 (\tilde{g}_m - \tilde{S}_m)$$
$$k_m = \mu^2 H (-\tilde{\epsilon}_{m1})$$
$$l_m = 0$$
$$n_m = \mu^2 H (-\tilde{\epsilon}_{m2})$$
$$o_m = 0$$

$$p_m = -\mu^2 H_{,x} \tilde{\epsilon}_{m1}$$

$$q_m = -\mu^2 H_{,x} \tilde{\epsilon}_{m2}$$

$$r_m = -\mu^2 \eta_{,t} \tilde{\epsilon}_{m1}$$

$$t_m = -\mu^2 \eta_{,t} \tilde{\epsilon}_{m2}$$

$$v_m = H \tilde{g}_m \tag{A.7}$$

For $m = 1, 2$, the coefficients are given as:

$$a_m = H g_m - \mu^2 h_{b,x} \eta_{,x} H g_m - \mu^2 h_{b,xx} H^2 (g_m - S_m)$$

$$b_m = -\mu^2 H^2 H_{,x} g_m - \mu^2 h_{b,x} H (g_m - S_m) + \mu^2 H^2 h_{b,x} S_m$$

$$c_m = \frac{-\mu^2}{2} H^3 (g_m - v_m)$$

$$d_m = H g_m - \mu^2 H \eta_{,x} h_{b,x} g_m + (3 h_{b,xx})\left(-\mu^2 H^2 (g_m - S_m)\right)$$

$$e_m = \mu^2 H^2 \eta_{,x} g_m$$

$$f_m = -\mu^2 H^2 \left(\eta_{,x} g_m + 2(g_m - S_m) h_{b,x}\right)$$

$$h_m = +\frac{\mu^2}{2} H^3 (g_m - v_m)$$

$$i_m = \frac{-\mu^2}{2} H^3 (g_m - v_m)$$

$$j_m = -\mu^2 H \eta_{,x} h_{b,xx} g_m - h_{b,xxx} \mu^2 H^2 (g_m - S_m)$$

$$k_m = \mu^2 H (\phi_{m1} - \epsilon_{m1})$$

$$l_m = \mu^2 H \phi_{m1}$$

$$n_m = \mu^2 H (\phi_{m2} - \epsilon_{m2})$$

$$o_m = \mu^2 H \phi_{m2}$$

$$p_m = -\mu^2 H_{,x} \epsilon_{m1}$$

$$q_m = -\mu^2 H_{,x} \epsilon_{m2}$$

$$r_m = -\mu^2 \eta_{,t} \epsilon_{m1}$$

$$t_m = -\mu^2 \eta_{,t} \epsilon_{m2}$$

$$v_m = H g_m \tag{A.8}$$

See [40] for obtaining $\tilde{}$ quantities of the integrals. We take $\mu = 1$ in all our computations.

References

[1] V. Aizinger, C. Dawson, A discontinuous Galerkin method for two-dimensional flow and transport in shallow water, Adv. Water Resour. 25 (1) (2002) 67–84.
[2] D.N. Arnold, et al., Unified analysis of discontinuous Galerkin methods for elliptic problems, SIAM J. Numer. Anal. 39 (5) (2002) 1749–1779.
[3] K. Atkinson, H. Weimin, Theoretical Numerical Analysis, vol. 39, Springer, 2005.
[4] F. Bassi, S. Rebay, A high order discontinuous Galerkin method for compressible turbulent flows, in: Discontinuous Galerkin Methods, Springer, Berlin, Heidelberg, 2000, pp. 77–88.
[5] S. Beji, J.A. Battjes, Experimental investigation of wave propagation over a bar, Coast. Eng. 19 (1) (1993) 151–162.
[6] P. Bonneton, et al., A splitting approach for the fully nonlinear and weakly dispersive Green–Naghdi model, J. Comput. Phys. 230 (4) (2011) 1479–1498.
[7] Susanne C. Brenner, R. Scott, The Mathematical Theory of Finite Element Methods, vol. 15, Springer, 2008.
[8] R.K.-C. Chan, R.L. Street, A computer study of finite-amplitude water waves, J. Comput. Phys. 6 (1) (1970) 68–94.
[9] B. Cockburn, G.E. Karniadakis, C.W. Shu, The Development of Discontinuous Galerkin Methods, Springer, 2000.
[10] B. Cockburn, C.W. Shu, The Runge–Kutta discontinuous Galerkin method for conservation laws V: multidimensional systems, J. Comput. Phys. 141 (2) (1998) 199–224.
[11] B. Cockburn, C.W. Shu, The local discontinuous Galerkin method for time-dependent convection–diffusion systems, SIAM J. Numer. Anal. 35 (6) (1998) 2440–2463.
[12] B. Cockburn, Discontinuous Galerkin methods, Z. Angew. Math. Mech. 83 (11) (2003) 731–754.
[13] C. Dawson, et al., Discontinuous Galerkin methods for modeling Hurricane storm surge, Adv. Water Resour. 34 (9) (2011) 1165–1176.
[14] R.G. Dean, R.A. Dalrymple, Water Wave Mechanics for Engineers and Scientists, World Scientific, 1991.
[15] M.W. Dingemans, Comparison of computations with Boussinesq-like models and laboratory measurements, Mast-G8M technical report H 1684, 1994.
[16] A.P. Engsig-Karup, Unstructured nodal DG-FEM solution of high-order Boussinesq-type equations, PhD thesis, Technical University, Denmark, 2006.
[17] A.P. Engsig-Karup, et al., Nodal DG-FEM solution of high-order Boussinesq-type equations, J. Eng. Math. 56 (3) (2006) 351–370.

[18] C. Eskilsson, S.J. Sherwin, Spectral hp discontinuous Galerkin methods for modelling 2D Boussinesq equations, J. Comput. Phys. 212 (2) (2006) 566–589.
[19] A.E. Green, P.M. Naghdi, A derivation of equations for wave propagation in water of variable depth, J. Fluid Mech. 78 (2) (1976) 237–246.
[20] M.F. Gobbi, J.T. Kirby, Wave evolution over submerged sills: tests of a high-order Boussinesq model, Coast. Eng. 37 (1) (1999) 57–96.
[21] J.S. Hesthaven, T. Warburton, Nodal Discontinuous Galerkin Methods: Algorithms, Analysis, and Applications, vol. 54, Springer-Verlag, New York, 2008.
[22] R.M. Kirby, G.E. Karniadakis, De-aliasing on non-uniform grids: algorithms and applications, J. Comput. Phys. 191 (1) (2003) 249–264.
[23] A.B. Kennedy, et al., Boussinesq modeling of wave transformation, breaking, and runup. I: 1D, J. Waterw. Port Coast. Ocean Eng. 126 (1) (2000) 39–47.
[24] A.B. Kennedy, J.T. Kirby, M.F. Gobbi, Simplified higher-order Boussinesq equations: I. Linear simplifications, Coast. Eng. 44 (3) (2002) 205–229.
[25] E.J. Kubatko, J.J. Westerink, C. Dawson, hp discontinuous Galerkin methods for advection dominated problems in shallow water flow, Comput. Methods Appl. Mech. Eng. 196 (1) (2006) 437–451.
[26] D. Lannes, P. Bonneton, Derivation of asymptotic two-dimensional time-dependent equations for surface water wave propagation, Phys. Fluids 21 (1) (2009) 016601.
[27] Per A. Madsen, Y. Agnon, Accuracy and convergence of velocity formulations for water waves in the framework of Boussinesq theory, J. Fluid Mech. 477 (1) (2003) 285–319.
[28] Per A. Madsen, Ole R. Sørensen, A new form of the Boussinesq equations with improved linear dispersion characteristics. Part 2. A slowly-varying bathymetry, Coast. Eng. 18 (3) (1992) 183–204.
[29] Per A. Madsen, O.R. Sørensen, H.A. Schäffer, Surf zone dynamics simulated by a Boussinesq type model. Part I. Model description and cross-shore motion of regular waves, Coast. Eng. 32 (4) (1997) 255–287.
[30] T. Maxworthy, Experiments on collisions between solitary waves, J. Fluid Mech. 76 (01) (1976) 177–186.
[31] O. Nwogu, Alternative form of Boussinesq equations for nearshore wave propagation, J. Waterw. Port Coast. Ocean Eng. 119 (6) (1993) 618–638.
[32] D.H. Peregrine, Long waves on a beach, J. Fluid Mech. 27 (1967) 815–827.
[33] H. Power, A.T. Chwang, On reflection of a planar solitary wave at a vertical wall, Wave Motion 6 (2) (1984) 183–195.
[34] F. Serre, Contribution à l'étude des écoulements permanents et variables dans les canaux, Houille Blanche 6 (1953) 830–872.
[35] H.A. Schäffer, Per A. Madsen, R. Deigaard, A Boussinesq model for waves breaking in shallow water, Coast. Eng. 20 (3) (1993) 185–202.
[36] J.J. Shields, W.C. Webster, On direct methods in water-wave theory, J. Fluid Mech. 197 (1) (1988) 171–199.
[37] C.H. Su, R.M. Mirie, On head-on collisions between two solitary waves, J. Fluid Mech. 98 (3) (1980) 509–525.
[38] W. Webster, D.Y. Kim, The dispersion of large-amplitude gravity waves in deep water, in: Naval Hydrodynamics 18th Symposium, National Academy Press, Washington DC, 1991, p. 397.
[39] J. Yan, C.W. Shu, A local discontinuous Galerkin method for KdV type equations, SIAM J. Numer. Anal. 40 (2) (2002) 769–791.
[40] Y. Zhang, et al., Boussinesq–Green–Naghdi rotational water wave theory, Coast. Eng. 73 (2013) 13–27.